Numerical Simulation of Three-Core Photonic Crystal Fiber With Large Group-Velocity Dispersion

JIANFANG YANG, CHUNCAN WANG, CAIPING JIA, AND MUGUANG WANG

Key Laboratory of All Optical Network and Advanced Telecommunication Network, Ministry of Education, Institute of Lightwave Technology, Beijing Jiaotong University, Beijing 100044, China

Corresponding author: Chuncan Wang (chcwang@bjtu.edu.cn)

ABSTRACT The three-core photonic crystal fiber (TC-PCF) is proposed to obtain large group-velocity dispersion (GVD) because of the coupling effects between the fundamental modes (FMs) of the central core and higher-order modes (HOMs) of the two side cores. The supermodes of the TC-PCF can provide concave anomalous- and normal-GVD profiles with large peak values at the maximum dispersion wavelengths (MDWs), which can be shifted in three wavelength windows of 1030 nm, 1550 nm and 1900 nm by properly tuning the refractive indexes of the cores or the air-hole diameters. Furthermore, the numerical results show that two segments of the TC-PCFs with large anomalous GVDs and opposite values of the third-order dispersion (TOD) can provide much higher efficiency of pulse compression than one segment of the TC-PCF. Additionally, the TC-PCFs with large normal GVDs can be used to stretch pulses due to their low nonlinearities and short fiber lengths.

INDEX TERMS Fiber nonlinear optics, optical fibers, optical pulse compression.

I. INTRODUCTION

A variety of optical devices with large anomalous and normal GVD have been proposed, mainly including bulky optical components and fiber-optic devices. First, bulky optical components, such as diffraction grating pairs [1] and prism pairs [2], exhibit large and tunable dispersion accompanied with low nonlinearity and loss. However, these optical components are usually bulky and need careful alignment. Second, the fiber components with large GVDs are suitable for the all-fiber compact systems. For example, it has been demonstrated experimentally that the chirped fiber Bragg grating operating in the reflection mode can be used for dispersion compensations due to its large dispersion and negligible nonlinear effects [3]–[5]. The dispersion-compensating fibers (DCFs) consisting of two highly asymmetric concentric cores have large normal GVDs ranging from some hundreds to thousands of ps/(nm·km) with an appropriate choice of the fiber parameters [6]–[8]. Moreover, the efficient dispersion managements were also demonstrated by properly designing the index-guiding and bandgap-guiding

silica photonic crystal fibers (PCFs). In particular, dual-concentric-core photonic crystal fibers (DCC-PCF) can provide large GVD at the desired wavelength by properly tuning the geometrical parameters [9]–[12]. Photonic bandgap fibers (PBGFs) including the solid-core photonic bandgap fibers (SC-PBGFs) [13], [14] and hollow-core photonic bandgap fibers (HC-PBGFs) [15], [16], can also show large GVD at both edges of its photonic bandgap. Recently, the hybrid multi-trench fiber (H-MTF) with two high-index cores (Ge-doped silica) positioned along the x-axis of the MTF, was proposed numerically to obtain an anomalous GVD of > 72 ps/(nm·km) at 1064 nm with large effective mode area (> 390 μm^2) [17].

In this paper, an alternative approach is proposed to obtain large normal and anomalous GVDs of the fiber based on the TC-PCF formed by one core in the center and two neighboring cores on the two sides surrounded by air-hole cladding. In Section 2, the properties of the TC-PCF including the GVD, nonlinear parameter and confinement loss, are presented, where the influences of the fiber parameters on the GVDs are discussed. Furthermore, the applications of the proposed TC-PCF are discussed by numerical simulations in Section 3.

The associate editor coordinating the review of this manuscript and approving it for publication was Sukhdev Roy.

II. THE PROPERTIES OF THE TC-PCF

Figure 1(a) shows the cross section of the TC-PCF, where the refractive index of the core A is lower than those of the core B to ensure the single-mode and multimode operations in the core A and core B, respectively. According to the coupled mode theory, the coupling between the nearest neighbor cores needs to be considered [18], [19]. As a result, the coupling effect for the TC-PCF in Fig. 1(a) essentially occurs between the two independent structures, i.e., the waveguide 1 (W1) with the core A and the waveguide 2 (W2) with the core B, as shown in Figs. 1(b) and (c), respectively. The mode coupling between the cores A and B in the TC-PCF can occur in the vicinity of index-matched wavelengths, where the propagation modes in two individual waveguides have the same effective refractive index [20]. Additionally, the cores and cladding of the proposed TC-PCF are made of Ge-doped silica and pure silica, and the fiber can be fabricated by using the stack-and-draw procedure [21].
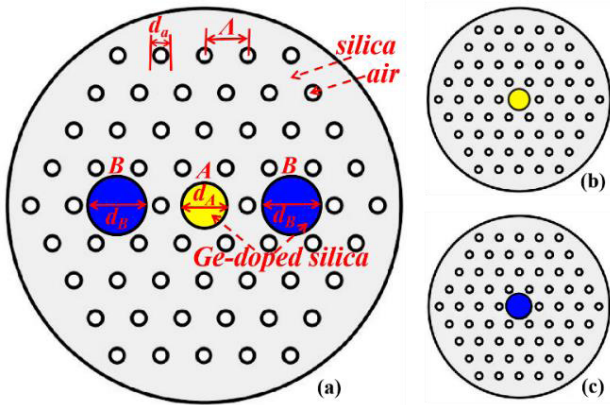

FIGURE 1. (a) Cross section of the TC-PCF. The host material is pure silica represented by gray color. The air hole in the cladding are arranged in a triangular configuration with the diameter d_a and pitch Λ. The refractive indexes of the cores A (yellow) and B (blue), i.e., n_A and n_B, are dependent of the GeO$_2$ concentration X mol%, where d_A and d_B represent the diameters of the cores A and B. Cross section of the waveguide 1 (W1) including the core A and waveguide 2 (W2) including the core B are shown in the Fig. 1(b) and 1(c).

A. THE CASE IN THE WAVELENGTH WINDOW OF 1550 nm

First, the properties of the TC-PCF are analyzed in the wavelength window of 1550 nm, which is the most common wavelength window in the field of optical fiber communications. The GVD parameter $D(\lambda)$ in the fiber is given by [22]

$$D\left(\lambda\right) = -\frac{\lambda}{c}\frac{d^2\mathrm{Re}\left(n_{eff}\right)}{d\lambda^2} \tag{1}$$

where $\mathrm{Re}(n_{eff})$ is the real part of the effective refractive index n_{eff} of the mode, c is the velocity of the light in vacuum, and λ is the operating wavelength. The material dispersions for the pure silica and Ge-doped silica are taken into account in the simulations by using the full-vector finite element method (FVFEM) solver Comsol. The refractive indexes in the pure silica and Ge-doped silica, i.e., n_{silica} and $n_{A,orB}$, are given
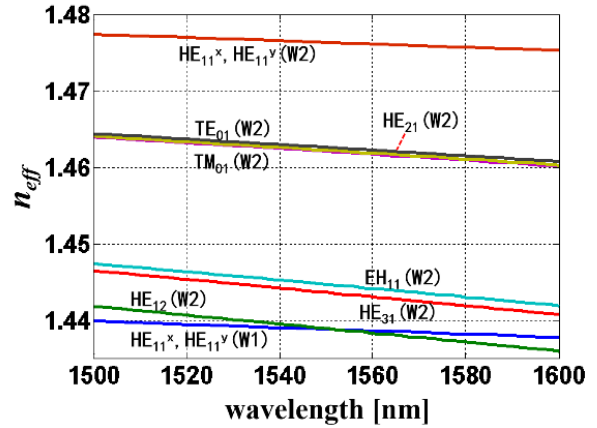

FIGURE 2. The curves of the effective refractive index n_{eff} for the modes in the W1 and W2, where $\Lambda = 4\ \mu m$, $d_A/\Lambda = 1$, $d_B/\Lambda = 1.5$, $d_a/\Lambda = 0.36$. The GeO$_2$ concentrations of the cores A and B are X_A and X_B in mol%, respectively. When $X_A = 2.35$ mol% and $X_B = 28$ mol%, $n_A = 1.4476$ and $n_B = 1.4855$, respectively.

by [23]

$$n_{silica}^2 = 1 + \sum_{i=1}^{3} \frac{SA_i\lambda^2}{\lambda^2 - SL_i^2} \tag{2}$$

$$n_{A,orB}^2 = 1 + \sum_{i=1}^{3} \frac{\left(SA_i + X\left(GA_i - SA_i\right)\right)\lambda^2}{\lambda^2 - \left(SL_i + X\left(GL_i - SL_i\right)\right)^2} \tag{3}$$

where the values of parameters SA_i, SL_i, GA_i, and GL_i are Sellmeier coefficients. The value of X is the GeO$_2$ concentration in mol%. In the following discussion, the value of X is tuned from 0.7 mol% and 30 mol%, which is feasible in practice because the GeO$_2$ concentration up to 75 mol% was demonstrated experimentally [24].

Since the mode intensity distributes in the Ge-doped silica areas with the different nonlinearity refractive index (NRI) $n_2(x, y)$, the nonlinear parameter $\gamma(\lambda)$ can be defined as

$$\gamma\left(\lambda\right) = \frac{2\pi}{\lambda} \frac{\int\int_{-\infty}^{\infty} n_2\left(x,y\right)\left|F\left(x,y\right)\right|^4 dxdy}{\left(\int\int_{-\infty}^{\infty}\left|F\left(x,y\right)\right|^2 dxdy\right)^2} \tag{4}$$

the NRIs in the silica and Ge-doped silica part are 2.2 and $(2.2+0.33X)$ with units of 10^{-20} m^2/W [25].

And the effective mode field area A_{eff} of the fiber is introduced as

$$A_{eff} = \frac{\left(\int\int_{-\infty}^{\infty}\left|F\left(x,y\right)\right|^2 dxdy\right)^2}{\int\int_{-\infty}^{\infty}\left|F\left(x,y\right)\right|^4 dxdy} \tag{5}$$

The confinement loss $L_C(\lambda)$ of the modes in the PCF can be defined by

$$L_C\left(\lambda\right) = \frac{20}{\ln\left(10\right)}\frac{2\pi}{\lambda}Im\left(n_{eff}\right) \tag{6}$$

where $Im(n_{eff})$ represents the imaginary part of the effective refractive index of the modes.

As shown in Fig. 2, the W1 supports only a pair of orthogonally polarized FMs, i.e., x- and y-polarized modes HE$_{11}^x$ and
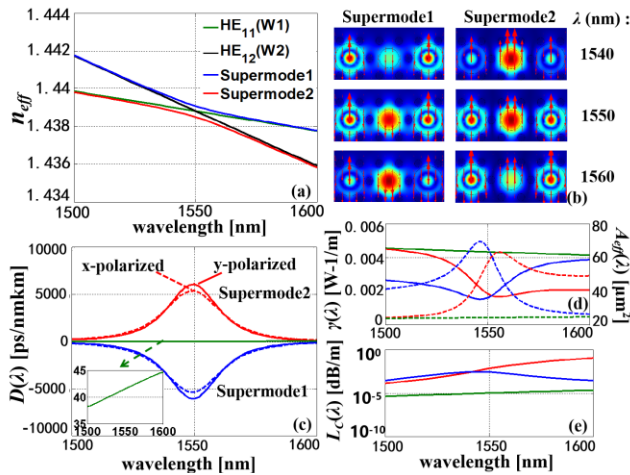
FIGURE 3. (a) The curves of the n_{eff} of the FMs HE_{11} (green) in the W1, modes HE_{12} (black) in the W2, and the supermodes 1 (blue) and 2 (red) for the TC-PCF versus wavelengths λ. (b) The mode intensity distributions of the supermodes 1 and 2 at wavelengths λ of 1540, 1550 and 1560 nm. (c) The GVD $D(\lambda)$ of the FMs HE_{11} in the W1 (green), supermodes 1 and 2 for the TC-PCF, where the solid and dash lines represent the supermodes corresponding to the y- and x-polarized modes HE_{11} in the core A, respectively. The nonlinear parameters $\gamma(\lambda)$ (solid lines) and effective mode field area $A_{eff}(\lambda)$ (dashed line) (d) and confinement losses $L_C(\lambda)$ (e) for the FMs HE_{11} in the W1, supermodes 1 and 2 in the TC-PCF, respectively.

FIGURE 4. (a) The curves of n_{eff} for the mode HE_{12} in the W2 and FMs HE_{11} in the W1 with different values of Δn_A as a function of wavelength λ, where the parameter Δn_A represents the index differences between the core A and pure silica, i.e., $\Delta n_A = n_A - n_{cladding}$, and $n_B = 1.4855$. For the supermodes in the TC-PCF, the curves of the GVD $D(\lambda)$ (b), the nonlinear parameter $\gamma(\lambda)$ (c) and confinement losses $L_C(\lambda)$ (d) for different values of Δn_A, respectively. The dash and solid lines represent the supermodes 1 and 2.

HE_{11}^y, while the W2 can support the FMs (HE_{11}^x and HE_{11}^y) and HOMs, that are the modes TE_{01}, TM_{01}, HE_{21}, EH_{11}, HE_{31} and HE_{12} in the sequence. The important point to note is that, an intersection of the n_{eff} curves between the orthogonally polarized FMs (HE_{11}^x and HE_{11}^y for the W1) and the higher-order modes HE_{12} for the W2 can be obtained at the wavelength of 1550 nm by tuning the fiber parameters properly. As a result, the mode coupling between the cores A and B in the TC-PCF occurs at 1550 nm. As shown in Fig. 3(a), a noteworthy feature is that when the wavelength is increased and close to the wavelength of 1550 nm, the values of n_{eff} for the supermodes 1 and 2 in the TC-PCF deviates from the n_{eff} curves of modes HE_{12} (W2) and HE_{11} (W1) due to the enhanced mode coupling effects between them, and then coincide with the n_{eff} curves of the modes HE_{11} and HE_{12} asymptotically with a further increase in the wavelengths. Since the mode intensity distributions of the supermodes with the y-polarized FM HE_{11}^y in the core A is similar to the case for the x-polarized FM HE_{11}^x, only the former case is shown in Fig. 3(b), where the mode intensity profiles of the supermodes 1 and 2 are shown at 1540, 1550 and 1560 nm, respectively. Furthermore, as shown in Fig. 3(c), the absolute values of the GVD for the supermodes 1 and 2 increase dramatically and symmetrically in the vicinity of 1550 nm because of the mode-coupling-induced waveguide dispersion [7]. The supermodes 1 and 2 exhibit large dispersion characteristics in the normal and anomalous GVD regimes, respectively. A noteworthy feature is that the absolute values of GVD attain its maximum values at the index-matched wavelength, which can also be called the maximum dispersion wavelength
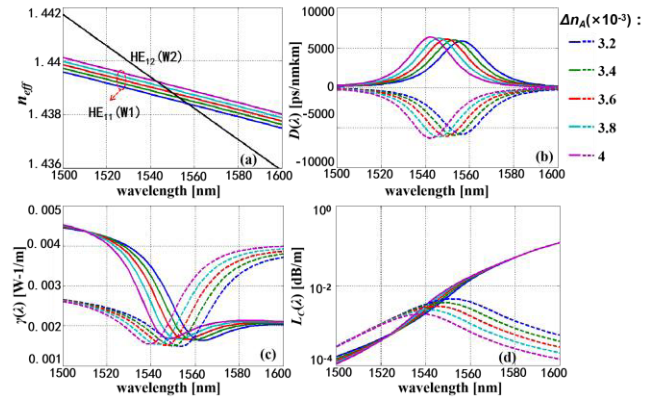
(MDW). For example, the values of GVD at the MDW for the supermodes 1 and 2 are –6075 and 6098 ps/(nm·km), which are much larger than the GVD of the W1 at 1550 nm, i.e., 41.63 ps/(nm·km). Since the results of the supermodes with the y-polarized modes in the core A region are generally identical to those of the supermodes with the x-polarized modes shown in Fig. 3(c), only the former case is considered in the following discussions.

Furthermore, as shown in Fig. 3(d), the values of the nonlinear parameter $\gamma(\lambda)$ are less than 0.005 W^{-1}/m in the wavelength range of 1500 – 1600 nm when $\Lambda = 4\ \mu m$, and reduced to below 0.002 W^{-1}/m at the MDW. The reason is that the effective mode field areas A_{eff} are increased near the MDWs due to the mode coupling between the cores A and B. Such low nonlinear parameter ensures that the evolutions of pulse along the fiber are less affected by the nonlinear effects. Additionally, as shown in Fig. 3(e), the confinement losses $L_C(\lambda)$ of both supermodes 1 and 2 can remain below 0.1 dB/m due to the air-hole cladding structure. And the loss can be reduced further by increasing the number of rings of air-hole cladding.

For the large GVD TC-PCF, it is also important to shift the MDW by tuning the fiber parameters. To ensure a single-mode operation of the W1 with the given air-hole diameter and pitch, the GeO_2 concentration in the core A is tuned within a relatively small range. As shown in Fig. 4(a), the n_{eff} curves of the FMs HE_{11} in the W1 shift down with a decrease of the GeO_2 concentration in the core A, resulting in an increase of the index-matched wavelength. The MDWs also shift toward the long wavelengths. As shown in Fig. 4(b), when the values of Δn_A are reduced from 4×10^{-3} to 3.2×10^{-3}, the MDWs shift from 1542 to 1557 nm. To extend further the wavelength tuning range of the MDWs, as shown in Fig. 5(a), a 2.4×10^{-3} increase in the n_B can result in relatively large wavelength shifts of the index-matched
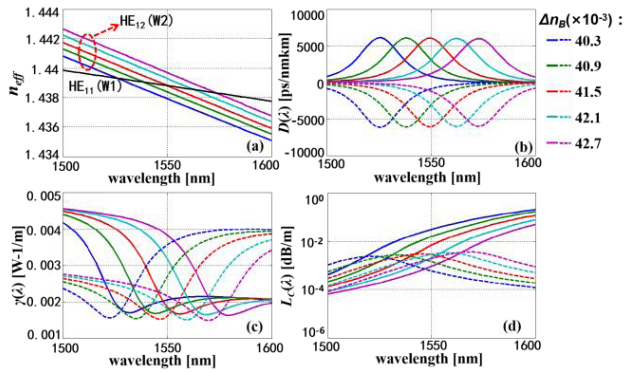
FIGURE 5. (a) The curves of the n_{eff} for the FMs HE_{11} in the W1 and modes HE_{12} in the W2 with different values of $\triangle n_B$ as a function of wavelength λ, where the parameter $\triangle n_B$ represents the index differences between the cores B and pure silica, i.e., $\triangle n_B = n_B - n_{cladding}$, and $n_A = 1.4476$. For the supermodes in the TC-PCF, the GVD $D(\lambda)$ (b), the nonlinear parameter $\gamma(\lambda)$ (c) and confinement losses $L_C(\lambda)$ (d) for different values of $\triangle n_B$. The dash and solid lines represent the supermodes 1 and 2.
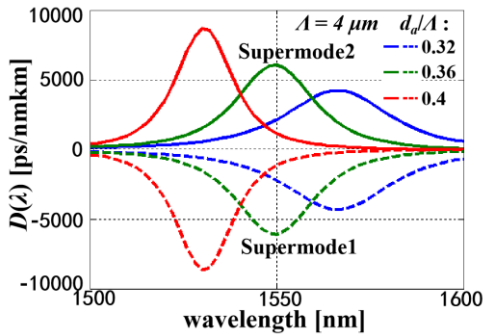

FIGURE 6. The curves of GVD $D(\lambda)$ for the supermodes 1 and 2 with different values of d_a/Λ. The values of Λ, n_A, n_B, d_A/Λ and d_B/Λ are identical to those in Fig. 2.

wavelengths between the modes HE_{11} (W1) and HE_{12} (W2). For this reason, as shown in Fig. 5(b), when the values of $\triangle n_B$ increase from 40.3×10^{-3} to 42.7×10^{-3}, the MDWs shift from 1526 nm to 1574 nm. Therefore, the large GVD characteristic with a desired MDW can be obtained in the 1550 nm window by properly tuning GeO$_2$ concentrations in the cores A or B. Additionally, it can be seen from Figs. 4 and 5 that when the GeO$_2$ concentrations decrease in the cores A and B, the curves of $\gamma(\lambda)$ and $L_C(\lambda)$ for the supermodes have a red and blue shift in the wavelength region, respectively. However, in both cases, the maximum values of the $\gamma(\lambda)$ and $L_C(\lambda)$ are limited below 0.005 W^{-1}/m and 0.1 dB/m.

Except for the refractive indexes in the cores A and B, the influence of d_a/Λ on the GVDs of the supermodes 1 and 2 are shown in Fig. 6. It can be seen that when the values of d_a/Λ increase from 0.32 to 0.4 and the other parameters remain unchanged, the GVD curves for both the supermodes 1 and 2 exhibit an increase of the absolute values of GVD at the MDW accompanied with a blue shift of the MDW and a narrowing of the GVD profile.

Since the effective mode field area (A_{eff}) of a PCF can be flexibly tuned by designing its air hole structure, the values
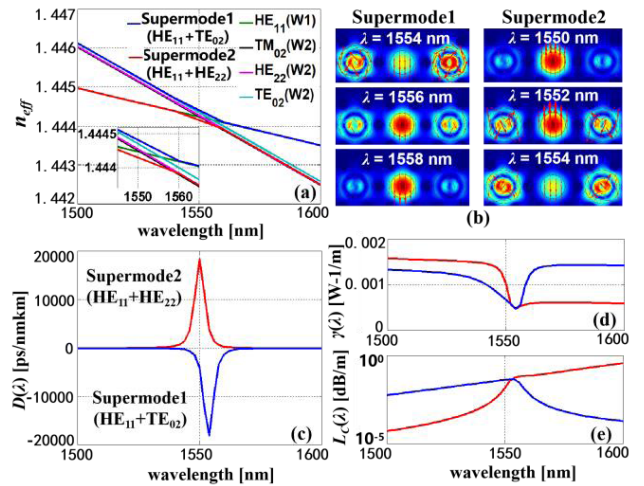

FIGURE 7. (a) The curves of the n_{eff} of the FMs HE_{11} (green) in the W1, modes TM_{02} (black), HE_{22} (pink) and TE_{02} (cyan) in the W2 versus wavelength λ when the air-hole pitch Λ is increased to 8 μm. (b) The mode filed distributions of the two supermodes formed by the mode couplings between the modes HE_{11}^y (W1) and TE_{02} (W2) at wavelengths λ of 1554, 1556 and 1558 nm, and between the modes HE_{11}^y (W1) and HE_{22} (W2) at wavelengths λ of 1550, 1552 and 1554 nm, respectively. The curves of the GVD $D(\lambda)$ (c), the nonlinear parameter $\gamma(\lambda)$ (d) and confinement losses $L_C(\lambda)$ (e) of the two supermodes in the TC-PCF, where $\Lambda = 8$ μm, $n_A = 1.4472$ and $n_B = 1.4675$. The values of d_A/Λ, d_B/Λ and d_a/Λ are identical to those in Fig. 2.

of A_{eff} can be increased to reduce the nonlinear parameter by increasing the air-hole spacing. When d_a/Λ remains to be 0.36 and the other geometric parameters are increased by a factor of 2, there are three intersections of the n_{eff} curves between the FMs HE_{11} in the W1 and the higher-order modes TE_{02}, TM_{02} and HE_{22} in the W2, that correspond to $\lambda = 1550.6$ nm for the mode TM_{02}, 1551.7 nm for the mode HE_{22} and 1555.7 nm for the mode TE_{02} in Fig. 7(a), respectively. Since the FMs HE_{11} are polarized in two orthogonal directions, the supermodes can be divided in two cases according to the mode fields with the x- and y-polarization in the core-A region. The former case corresponds to the mode couplings occur between the modes HE_{11}^x and TM_{02}, and HE_{11}^x and HE_{22}, while the latter case corresponds to the coupling between the HE_{11}^y and TE_{02}, and HE_{11}^y and HE_{22} modes shown in Fig. 7(b). Furthermore, as shown in Fig. 7(c), when mode coupling happens between the HE_{11}^y and HE_{22} modes, the supermode 2 in the TC-PCF has a large anomalous GVD, while the supermode 1 with the coupling between the HE_{11}^y and TE_{02} modes exhibits a large normal GVD. As a result, the peak values of the normal and anomalous GVD are -18130 ps/(nm·km) at 1554 nm and 18380 ps/(nm·km) at 1550 nm, respectively. However, the wavelength bandwidths of the full width at half maximum GVD are much narrower than those in the Figs. 4 and 5. The results indicate that a trade-off exists between the maximum values of the GVD and the wavelength bandwidths for the TC-PCF. Additionally, as the air hole pitch is increased to 8 μm, the values of the nonlinear coefficient $\gamma(\lambda)$ are reduced below 0.002 W^{-1}/m in the wavelength range of 1500–1600 nm,
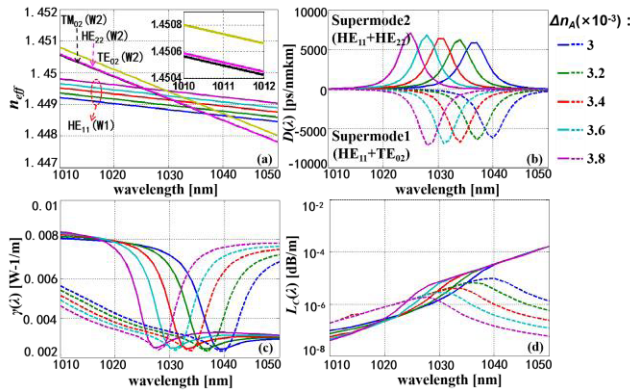
FIGURE 8. The curves of n_{eff} for the higher-order modes TE_{02}, HE_{22} and TM_{02} in the W2 and FMs HE_{11} in the W1 with different values of Δn_A as a function of wavelength λ. For the supermodes in the TC-PCF, the curves of the GVD $D(\lambda)$ (b), the nonlinear parameter $\gamma(\lambda)$ (c) and confinement losses $L_C(\lambda)$ (d) for the different values of Δn_A, respectively. The values of Λ, d_A/Λ, d_B/Λ and d_a/Λ are identical to those in Fig. 2, and $n_B = 1.4854$. The dash and solid lines represent the supermodes 1 and 2.

especially 0.0005 W^{-1}/m near the MDW show in Fig. 7(d). Thus the effects of nonlinearity on the pulse evolutions can be weak enough. The corresponding confinement losses $L_C(\lambda)$ shown in Fig. 7(e) can remain below 0.4 dB/m.

B. THE CASES IN THE WAVELENGTH WINDOWS OF 1030 AND 1900 nm

Except for the 1550 nm window, the pulse laser sources based on the Yb- and Tm-doped fiber lasers operate in the 1030 nm and 1900 nm windows. For this reason, the TC-PCF with the large GVD are discussed in the two wavelength windows. As shown in Fig. 8(a), in the case of 1030 nm with an appropriate choice of fiber parameters, the FMs of the core A can couple with the higher-order modes TE_{02}, TM_{02}, HE_{22} of the core B. For example, when $\Delta n_A = 3.4 \times 10^{-3}$, the intersections exist between the n_{eff} curves of the FMs (W1) and the higher-order modes (W2), where the index-matched wavelengths are 1030.9 nm for the TM_{02} mode, 1031.1 nm for the HE_{22} modes, and 1035.3 nm for the TE_{02} mode, respectively. At the same time, the effects of tuning GeO_2 concentration of the core A on dispersion characteristics are shown in Fig. 8(b). The MDWs can shift from 1025 nm to 1037 nm, and the maximum values of the GVD at 1030 nm can reach 25560 ps/(nm·km) in the anomalous dispersion regime and –27570 ps/(nm·km) in the normal dispersion regime. Additionally, as shown in Fig. 8(c), the values of the $\gamma(\lambda)$ can be reduced around 0.003 W^{-1}/m at the MDWs, where the confinement losses $L_C(\lambda)$ are below 1×10^{-4} dB/m shown in Fig. 8(d).

Furthermore, the similar results for the TC-PCF can be obtained in the 1900 nm window. As shown in Fig. 9, when the values of Δn_A increase from 1.3×10^{-3} to 2.1×10^{-3}, the MDWs shift from 1914 to 1888 nm, and the peak and dip values of the GVD curves at 1900 nm are 7799 ps/(nm·km) and –8235 ps/(nm·km) in the anomalous and normal dispersion regimes, respectively. Meanwhile, it can be seen that

the $\gamma(\lambda)$ and $L_C(\lambda)$ are low enough in the wavelength range of 1850–1950 nm.

III. APPLICATIONS OF THE TC-PCF WITH THE LARGE GVD
The designed TC-PCFs have large values of the GVD both in the normal and anomalous dispersion regimes, while the nonlinear parameters and confinement losses are low enough. This result implies the potential applications of the TC-PCF consisting of pulse compression in the anomalous GVD regime, and pulse broadening in the normal GVD regime. The evolutions of the pulse along the fiber can be described through solving the generalized nonlinear Schrödinger equation (GNLSE) [25]:

$$\frac{\partial A}{\partial z} + \frac{\alpha}{2}A - \sum_{k \geq 2} \frac{i^{k+1}}{k!} \beta_k \frac{\partial^k A}{\partial T^k} = i\gamma \left(1 + i\frac{\partial}{\partial T}\right)$$
$$\cdot \left[A(z, T) \int_{-\infty}^{\infty} R(T') \left|A(z, T - T')\right|^2 dT'\right] \quad (7)$$

where $A(z, T)$ is the slowly varying amplitude of the pulse envelope in the time domain, T is the retarded time for a comoving frame at the envelope group velocity $1/\beta_1$, α is the linear loss, β_k are the dispersion coefficients associated with the Taylor series expansion of the propagation constant $\beta(\omega)$ around the center frequency ω_0. In the process of solving GNLSE, the dispersion operator in the frequency domain is applied through multiplication of the complex spectral envelope $\tilde{A}(z, \omega)$ by the operator $\beta(\omega) - (\omega - \omega_0)\beta_1 - \beta_0$. The nonlinear response function $R(T) = (1 - f_R)\delta(T) + f_R h_R(T)$ includes both instantaneous and delayed Raman contributions. The fractional contribution of the delayed Raman response to nonlinear polarization f_R is taken to be 0.18. In the following simulations, the initial pulse is set to be a linearly chirped Gaussian pulse $A_0(T) = \sqrt{P_0} \exp\left(-(1 + iC)T^2/2T_0^2\right)$, where $T_0 = T_{FWHM}/2\sqrt{2\ln 2}$, and T_{FWHM} is the full width at half maximum (FWHM) pulse duration, C is the chirp parameter. The peak power P_0 can be obtained by $P_0 = 0.94E_0/T_{FWHM}$, where E_0 is the pulse energy. The linearly and positively chirped ($C > 0$) pulses with nearly Gaussian profiles can be generated by a passively mode-locked fiber lasers in the normal-dispersion regime [26]. The positively chirped Gaussian pulses can evolve to become chirp-free and negatively chirped pulses in the anomalous-dispersion regime if the nonlinearity-induced pulse distortions are negligible. The dispersion length L_D and the nonlinear length L_{NL} are given as

$$L_D = \frac{T_0^2}{|\beta_2|} \quad (8)$$

$$L_{NL} = \frac{1}{\gamma P_0} \quad (9)$$

where β_2 is the second-order dispersion. Depending on the relative magnitudes of L_D, L_{NL}, and the fiber length L, either dispersive or nonlinear effects may dominate along the fiber.
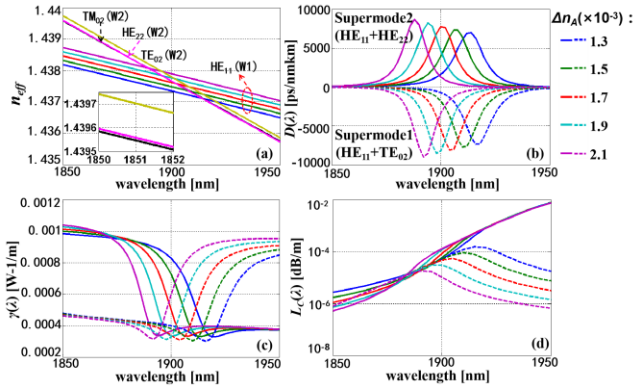
FIGURE 9. The curves of n_{eff} for the higher-order modes TE$_{02}$, HE$_{22}$ and TM$_{02}$ in the W2 and FMs HE$_{11}$ in the W1 with different values of Δn_A as a function of wavelength λ. For the supermodes in the TC-PCF, the curves of the GVD D(λ) (b), nonlinear parameter $\gamma(\lambda)$ (c) and confinement losses $L_C(\lambda)$ (d) for different values of Δn_A, respectively. The values of d_A/Λ, d_B/Λ and d_a/Λ are identical to those in Fig. 2. $\Lambda = 8 \ \mu m$ and $n_B = 1.4685$. The dash and solid lines represent the supermodes 1 and 2.
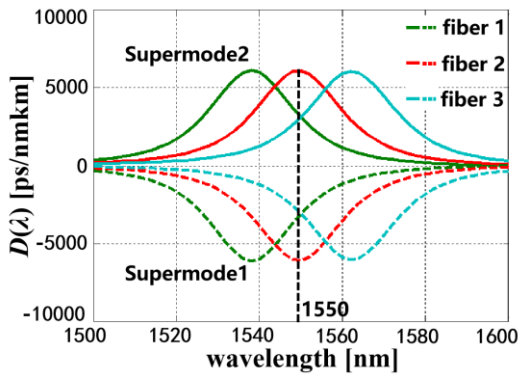

FIGURE 10. Three groups of dispersion curves represented by green, red and cyan-blue colors, corresponding to $\delta n_B = 40.9, 41.5, 42.1$ ($\times 10$-3) from Fig. 5(b), respectively.

A. DISCUSSIONS OF THE PULSE COMPRESSION IN THE ANOMALOUS DISPERSION REGIME

As shown in Fig. 10, the TC-PCF with appropriate parameters can support supermodes 1 and 2 with the large normal and anomalous GVDs in the 1550 nm window, respectively. For example, the fiber 2 with $\Delta n_B = 41.5 \times 10^{-3}$ can provide relatively flat GVD profiles with the GVD values of -6075 and 6098 ps/(nm·km) at the MDW of 1550nm for the supermodes 1 and 2, respectively. Moreover, the nonlinear parameters $\gamma(\lambda)$ are 2×10^{-3} and 1.5×10^{-3} W^{-1}/m, and the confinement losses $L_C(\lambda)$ are 0.003 and 0.007 dB/m at 1550 nm, respectively. For the fibers 1 (green) and 3 (cyan), the third-order dispersions (TOD) of these two fibers are nearly identical in magnitude with opposite signs at 1550 nm. This result indicates that the TOD effects of the two fibers can be cancelled in the vicinity of 1550 nm when the pulse passes through these two fiber segments with equal fiber lengths.

For the purpose of estimating the efficiency and quality of pulse compression, the compression factor F_C and the quality factor Q_C can be defined as

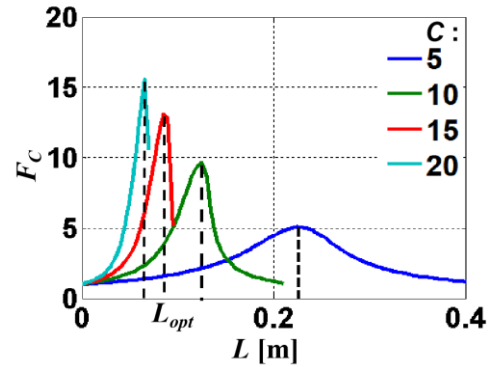$$F_C = \frac{T^C_{FWHM}}{T_{FWHM}} \tag{10}$$

FIGURE 11. For the initial pulses with different initial chirp parameters C, the curves of the compression factor FC as a function of the fiber length L, where Lopt = 0.064, 0.085, 0.12 and 0.225 m for C = 5, 10, 15 and 20, respectively. The center wavelength of the initial pulse is defined as λ_0. For the initial pulse, $\lambda_0 = 1550$ nm, TFWHM = 5 ps and E0 = 1 nJ.
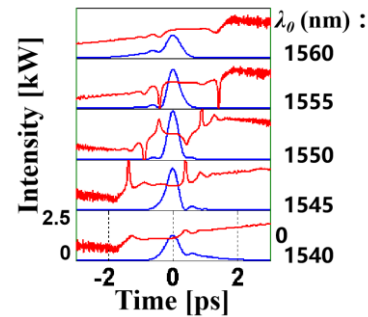

FIGURE 12. The intensity (blue) and chirp (red) profiles of the compressed pulses for the initial pulses with different central wavelengths λ_0, where TFWHM = 5ps, E0 = 1 nJ and C = 15.

$$Q_C = \frac{E_C}{E_{total}} \tag{11}$$

where T^C_{FWHM} is the full width at half maximum (FWHM) of the compressed pulse, E_{total} is the total energy of the compressed pulse, and E_C is the pulse energy contained in the central part of the compressed pulse.

When only the supermode 2 is excited in the fiber 2 by the input pulses with positive chirp parameters ($C > 0$), the pulses will undergo an initial narrowing stage because that the linearly positive chirp of the input pulse can be cancelled by the GVD-induced chirp ($\beta_2 < 0$), and then broadening with a further propagation. For this reason, as shown in Fig. 11, the input pulses with different chirp parameters can obtain the maximum compression factors at optimal fiber lengths L_{opt}, where the initial chirp of the pulse can be cancelled exactly. Additionally, when the chirp parameter C increases from 5 to 20, the maximum compression factor F_C increases from 5 to 15 with decreasing the optimal fiber length L_{opt} mainly because the spectral widths of the input pulses increase with the chirp parameters.

When the center wavelength λ_0 of the initial pulse deviates from the MDW, the TOD effects distort the compressed pulse such that the pulse becomes asymmetric with an oscillatory structure near one of its edges shown in Fig. 12. In the cases of $\lambda_0 = 1545$ and 1540 nm, the temporal oscillations appear
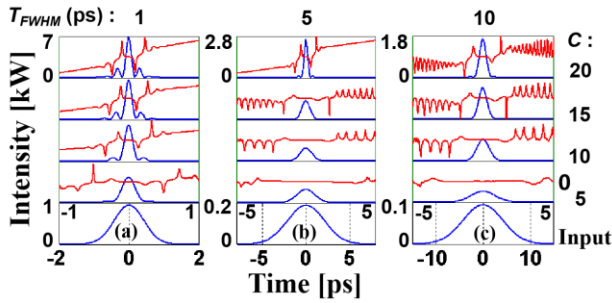
FIGURE 13. (a) The intensity and chirp profiles of the compressed pulse at the fiber 2 output with the optimal fiber length Lopt for different initial chirp C when initial pulse width TFWHM = 1 (a), 5 (b), 10 ps (c). For the initial pulse, E0 = 1 nJ and λ_0 = 1550 nm.

near the trailing pulse edge due to the positive β_3 when $\lambda_0 <$ MDW. When $\lambda_0 = 1555$ and 1560 nm ($\beta_3 < 0$), it is the leading pulse edge that develops oscillations.

Furthermore, the intensity and chirp profiles for the input and output pulses at the output end of the fiber 2 with $L = L_{opt}$ are shown in Fig. 13, where three cases of initial pulse widths $T_{FWHM} = 1, 5$ and 10 ps are presented. The 1-, 5- and 10-ps pulses with $C = 20$ can be compressed down to 90, 322 and 557 fs with compression factors F_C of around 11, 16 and 18 when the L_{opt} are 0.0047, 0.0656, 0.241 m and the nonlinear length L_{NL} are 0.57, 2.87, 5.73 m, respectively. Consequently, the pulses can be compressed to make them nearly chirp-free in the linear regime because that the fiber lengths are much shorter than the nonlinear lengths. However, the pedestals appear on both sides of the compressed pulses when the chirp parameter C increases mainly because the effects of the higher-order dispersions on the quality of compression become more important with an increase of pulse bandwidth. Especially for the case of $T_{FWHM} = 1$ ps with $C = 20$, the quality of compression degrade when the pedestals contain about 37% of the total pulse energy.

Alternatively, the positive-chirp pulse with central wavelength of 1550 nm can also be compressed through two segment fibers, i.e., the fiber 1 and 3. As shown in Fig. 10, the two GVD curves of the supermodes 2 in the fiber 1 and 3 have intersection at 1550 nm, where the values of the third-order dispersion (TOD) are -0.4659 (β_3 for the fiber 1) and 0.4523 ps³/m (β_3 for fiber 3), respectively. The TOD compensation condition is given by

$$\beta_{31}L_1 + \beta_{33}L_3 = 0 \qquad (12)$$

where β_{31} and β_{33} are the TOD parameters for the fibers 1 and 3 of fiber lengths L_1 and L_3, respectively. Additionally, the positions and sizes of the cores A and B for the two fibers are identical, which is helpful to obtain the low coupling loss and easy alignment between the two sections of fibers by using the optical fiber fusion splicer. Free space coupling is also feasible but with a relatively high coupling loss.

As shown in Fig. 14, when the initial pulse goes through the fiber 1 firstly, the output pulse becomes asymmetric and has a long tail on the leading side due to the negative TOD.
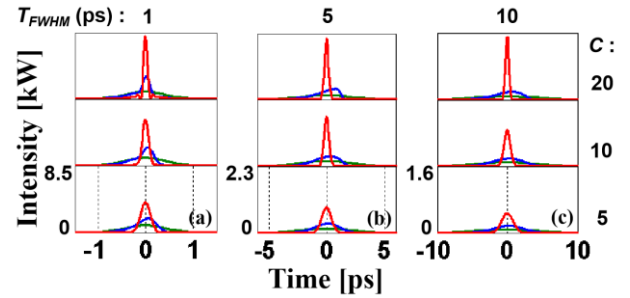

FIGURE 14. (a) The intensity profiles of the initial pulse (green), output pulses at the fibers 1 (blue) and 3 (red) ends for different chirp parameters C when initial pulse width TFWHM = 1 (a), 5 (b) and 10 ps (c). For the initial pulse, λ_0 = 1550 nm and E0 = 1 nJ.
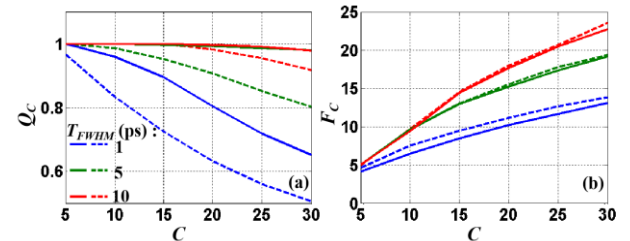

FIGURE 15. The curves of the quality factor QC (a) and compression factor FC (b) as a function of the chirp parameters C when initial pulse width TFWHM = 1, 5 and 10 ps in the case of the one-fiber-segment compression scheme (dashed line) and two-fiber-segments scheme (solid line).

And then through the fiber 3 of the same length as the fiber 1, the output pulse becomes symmetrical and well compressed, where both the positive chirp and TOD of the fiber 1 are compensated in this way. For example, for the 1-, 5- and 10-ps input pulses with $C = 20$, 98-, 386- and 635-fs compressed pulse with compression factors of 10, 13 and 16 can be obtained by using the fiber 1 and 3 of equal lengths 0.0024, 0.05 and 0.23 m, respectively. The total lengths of the two fibers are much shorter than the corresponding nonlinear lengths of 0.6, 3.0 and 6.0 m, which ensures pulse compressions in the linear regime.

For the above two pulse compression schemes, the quality factor Q_C and the compression factor F_C for different chirp parameters C and initial pulse widths T_{FWHM} are shown in Fig. 15. In the one-fiber-segment compression scheme, the values of Q_C decrease significantly with an increase of C, and drop to 0.51, 0.8, and 0.92 for 1-, 5- and 10-ps pulse with $C = 30$. For the two-fiber-segments scheme, Q_C remains > 0.97 for the 5- and 10-ps initial pulses except for the 1-ps pulse case, where Q_C drops to 0.65 when $C = 30$. The reason is that, when the bandwidth of the compressed pulse becomes comparable to or broader than the central flat part of the GVD curves near the MDW with increasing C and decreasing T_{FWHM}, the pulse distortion induced by the effect of the TOD becomes strong and then results in a decrease of Q_C. Moreover, the curves of F_C in both cases are almost identical for input pulses with the same parameters. Consequently, the two-fiber-segments pulse compression presents a better
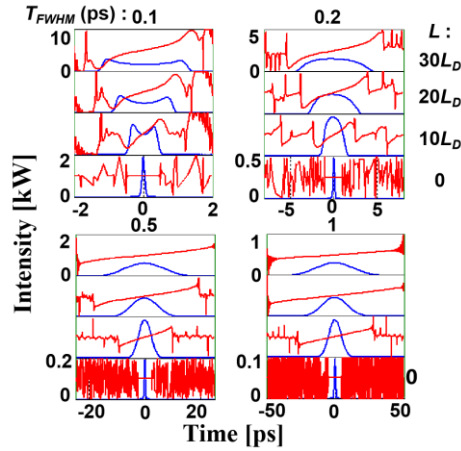
FIGURE 16. The intensity and chirp profiles of the input and output pulses at the end of the fiber 2 with different lengths L when initial pulse width TFWHM = 0.1, 0.2, 0.5 and 1ps. For the initial pulse, λ_0 = 1550 nm and E0 = 1 nJ.

quality of compression compared with the one-fiber-segment scheme mainly because of the compensation of both GVD and TOD over the entire bandwidth of the pulse.

B. DISCUSSIONS OF THE PULSE STRETCHER IN THE NORMAL DISPERSION REGIME

Since the supermode 1 of the TC-PCF can provide large normal GVD, the fiber can offer a potential application in the pulse stretcher. As shown in Fig. 16, when the unchirped Gaussian pulses ($C = 0$) input the fiber 2 and propagate as the supermode 1, the pulse can be broadened due to the effects of large normal GVD. For example, the output pulse can be temporally broadened with little distortion in the pulse shape when the pulse width T_{FWHM} for the 1-nJ input pulse is longer than 0.2 ps. In the case of $T_{FWHM} = 0.5$ ps, the nonlinear length L_{NL} is 0.332 m, the dispersion length L_D is 0.012 m. When L increases from $10L_D$ to $30L_D$, L is much shorter than L_{NL}. Thus the GVD-induced pulse broadening dominates the process of the pulse evolution. For the 0.1-ps input pulse with $L_D = 4.66 \times 10^{-4}$ m and $L_{NL} = 0.067$ m, the intensity profile of the output pulse has a nearly square shape mainly because of the combined effects of the normal GVD and self-phase modulation (SPM).

For the purpose of estimating the efficiency of pulse broadening, the broadening factor F_b can be defined as

$$F_b = \frac{T^b_{FWHM}}{T_{FWHM}} \tag{13}$$

where T^b_{FWHM} is the temporal FWHM of the broadened pulse. For initial unchirped Gaussian pulses, the extent of GVD-induced broadening is governed by the dispersion length L_D, and output pulse width can be expressed as [25]

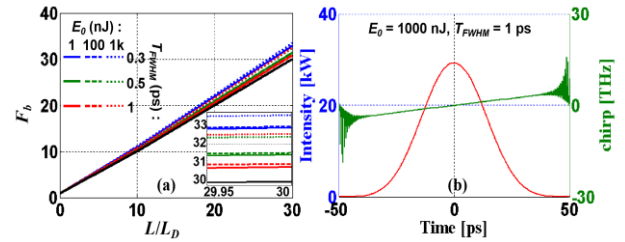$$T_1(z) = T_0 \left[1 + (z/L_D)^2 \right]^{1/2} \tag{14}$$

FIGURE 17. (a) Variation of pulse broadening factor F_b for different values of pulse energy E_0 and T_{FWHM} as a function of L/L_D. And the theoretical broadening factor is represented by a solid black line. The intensity and chirp profiles of the 1-ps pulse with 1000 nJ energy are shown in Fig. 17(b).

Thus the broadening factor F^1_b in theory can also be given by

$$F^1_b = \left[1 + (z/L_D)^2 \right]^{1/2} \tag{15}$$

As shown in Fig. 17, the curve of F^1_b obtained from Eq. (15) is slightly lower than those obtained from Eq. (13) because the influences of the peak-power-dependent SPM on the pulse evolutions are neglected in the former case. For a given fiber length L, the values of F_b increase slightly as the width T_{FWHM} of the initial pulse decreases from 1 to 0.3 ps. Moreover, the values of F_b remain nearly unchanged when the pulse energy increases from 1 to 1000 nJ because the fiber with a low nonlinear parameter is so short that the nonlinear effects are negligible. For this reason, the broadened pulse has a linear chirp across the entire pulse even when the pulse energy E_0 reaches 1000 nJ.

IV. CONCLUSION

An approach based on the TC-PCF is proposed to obtain the large GVD in the fiber. The supermodes of the TC-PCFs with appropriate parameters can exhibit concave dispersion profiles with large normal and anomalous GVD in three wavelength windows of 1030 nm, 1550 nm and 1900 nm. At the same time, the values of the nonlinear parameter $\gamma(\lambda)$ can be reduced below 0.003 W^{-1}/m at the MDWs in all three wavelength windows. Moreover, the MDW can be shifted over a wide wavelength range by properly tuning the air-hole diameter d_a and GeO$_2$ concentrations in the cores A or B for a given air-hole pitch Λ. Furthermore, the potential applications of the TC-PCF are discussed in the anomalous and normal GVD regimes by numerically solving the GNLSE. For the former case, the linearly chirped pulses with positive chirp parameters can be compressed by factors of >10 through one TC-PCF segment with the central wavelength λ_0 of the input pulse equal to the MDW, or through two TC-PCF segments with opposite values of TOD at λ_0. The numerical results show that the pedestals of the compressed pulses contain more pulse energies with an increase of the pulse bandwidth due to the TOD effects. However, the two-fiber-segments pulse compression has a better quality of compression than the one-fiber-segment scheme mainly because of the compen-

sation of both GVD and TOD over the entire bandwidth of the pulse. In the latter case, the output pulse can be temporally broadened monotonically as the fiber length increases, and the broadened pulses remain nearly undistorted with increasing pulse energies due to the relatively low nonlinearities and short fiber lengths for the TC-PCFs.

REFERENCES

[1] E. Treacy, "Optical pulse compression with diffraction gratings," *IEEE J. Quantum Electron.*, vol. QE-5, no. 9, pp. 454–458, Sep. 1969.

[2] R. L. Fork, O. E. Martinez, and J. P. Gordon, "Negative dispersion using pairs of prisms," *Opt. Lett.*, vol. 9, no. 5, pp. 150–152, May 1984.

[3] S. Kivistö, R. Herda, and O. G. Okhotnikov, "All-fiber supercontinuum source based on a mode-locked ytterbium laser with dispersion compensation by linearly chirped Bragg grating," *Opt. Express*, vol. 16, no. 1, pp. 265–270 , Jan. 2008.

[4] K. O. Hill, F. Bilodeau, B. Malo, T. Kitagawa, S. Theriault, D. C. Johnson, J. Albert, and K. Takiguchi, "Chirped in-fiber Bragg grating for compensation of optical-fiber dispersion," *Opt. Lett.*, vol. 19, no. 17, pp. 1314–1316, Sep. 1994.

[5] R. Kashyap, S. V. Chernikov, J. R. Taylor, and P. F. McKee, "30 ps chromatic dispersion compensation of 400 fs pulses at 100 Gbits/s in optical fibres using an all fibre photoinduced chirped reflection grating," *Electron. Lett.*, vol. 30, no. 13, pp. 1078–1080, Jun. 1994.

[6] K. Thyagarajan, R. K. Varshney, P. Palai, A. K. Ghatak, and I. C. Goyal, "A novel design of a dispersion compensating fiber," *IEEE Photon. Technol. Lett.*, vol. 8, no. 11, pp. 1510–1512, Nov. 1996.

[7] F. Gerome, J.-L. Auguste, J. Maury, J.-M. Blondy, and J. Marcou, "Theoretical and experimental analysis of a chromatic dispersion compensating module using a dual concentric core fiber," *J. Lightw. Technol.*, vol. 24, no. 1, pp. 442–448, Jan. 2006.

[8] T. Sakamoto, T. Matsui, K. Tsujikawa, and S. Tomita, "Hole-assisted dual concentric core fiber with ultralarge negative dispersion coefficient of-13,200 ps/nm/km," *Appl. Opt.*, vol. 50, no. 18, pp. 2979–2983, Jun. 2011.

[9] T. Fujisawa, K. Saitoh, K. Wada, and M. Koshiba, "Chromatic dispersion profile optimization of dual-concentric-core photonic crystal fibers for broadband dispersion compensation," *Opt. Express*, vol. 14, no. 2, pp. 893–900, Oct. 2006.

[10] D. C. Zografopoulos, C. Vázquez, E. E. Kriezis, and T. V. Yioultsis, "Dual-core photonic crystal fibers for tunable polarization mode dispersion compensation," *Opt. Express*, vol. 19, no. 22, pp. 21680–21691, Oct. 2011.

[11] P. S. Maji and P. Roy Chaudhuri, "Design of ultra large negative dispersion PCF with selectively tunable liquid infiltration for dispersion compensation," *Opt. Commun.*, vol. 325, pp. 134–143, Aug. 2014.

[12] S. Yang, Y. Zhang, X. Peng, Y. Lu, S. Xie, J. Li, W. Chen, Z. Jiang, J. Peng, and H. Li, "Theoretical study and experimental fabrication of high negative dispersion photonic crystal fiber with large area mode field," *Opt. Express*, vol. 14, no. 7, pp. 3015–3023, May 2006.

[13] A. Isomäki and O. G. Okhotnikov, "All-fiber ytterbium soliton mode-locked laser with dispersion control by solid-core photonic bandgap fiber," *Opt. Express*, vol. 14, no. 10, pp. 4368–4373, May 2006.

[14] Q. Fang, Z. Wang, L. Jin, J. Liu, Y. Yue, Y. Liu, G. Kai, S. Yuan, and X. Dong, "Dispersion design of all-solid photonic bandgap fiber," *J. Opt. Soc. Amer. B, Opt. Phys.*, vol. 24, no. 11, pp. 2899–2905, Nov. 2007.

[15] G. Bouwmans, F. Luan, J. Knight, P. St. J. Russell, L. Farr, B. Mangan, and H. Sabert, "Properties of a hollow-core photonic bandgap fiber at 850 nm wavelength," *Opt. Express*, vol. 11, no. 14, pp. 1613–1620, Jul. 2003.

[16] D. G. Ouzounov, F. R. Ahmad, D. Müller, N. Venkataraman, M. T. Gallagher, M. G. Thomas, J. Silcox, K. W. Koch, and A. L. Gaeta, "Generation of megawatt optical solitons in hollow-core photonic band-gap fibers," *Science*, vol. 301, no. 5640, pp. 1702–1704, Oct. 2003.

[17] D. Jain, C. Baskiotis, and J. K. Sahu, "Large mode area hybrid multi-trench fiber for anomalous dispersion," in *Proc. IEEE Conf. Opt. Fibre Commun. (OFC)*, Mar. 2014, pp. 1–3, Paper Th2A.40.

[18] A. Hardy and W. Streifer, "Coupled mode theory of parallel waveguides," *J. Lightw. Technol.*, vol. 3, no. 5, pp. 1135–1146, Nov. 1985.

[19] A. Mafi and J. V. Moloney, "Shaping modes in multicore photonic crystal fibers," *IEEE Photon. Technol. Lett.*, vol. 17, no. 2, pp. 348–350, Feb. 2005.

[20] J. Li, Y. Mao, C. Lu, H. Y. Tam, and P. K. A. Wai, "Polarizing properties of photonic crystal fibers with high-index cladding defects," *J. Lightw. Technol.*, vol. 28, no. 11, pp. 1608–1614, Jun. 2010.

[21] S. A. Cerqueira, Jr., F. Luan, C. M. B. Cordeiro, A. K. George, and J. C. Knight, "Hybrid photonic crystal fiber," *Opt. Express*, vol. 14, no. 2, pp. 926–931, Jan. 2006.

[22] A. Ferrando, E. Silvestre, J. J. Miret, P. Andrés, and M. V. Andrés, "Full-vector analysis of a realistic photonic crystal fiber," *Opt. Lett.*, vol. 24, no. 5, pp. 276–278, Mar. 1999.

[23] J. W. Fleming, "Dispersion in GeO$_2$-SiO$_2$ glasses," *Appl. Opt.*, vol. 23, no. 24, pp. 4486–4493, Oct. 1984.

[24] O. I. Medvedkov, S. A. Vasiliev, P. I. Gnusin, and E. M. Dianov, "Photosensitivity of optical fibers with extremely high germanium concentration," *Opt. Mater. Express*, vol. 2, no. 11, pp. 1478–1489, Nov. 2012.

[25] G. P. Agrawal, "Pulse propagation in fibers," in *Nonlinear Fiber Optics*, 5nd ed. San Francisco, CA, USA: Academic, 2013, pp. 27–56.

[26] A. Ruehl, O. Prochnow, D. Wandt, D. Kracht, B. Burgoyne, N. Godbout, and S. Lacroix, "Dynamics of parabolic pulses in an ultrafast fiber laser," *Opt. Lett.*, vol. 31, no. 18, pp. 2734–2736, Sep. 2006.

JIANFANG YANG received the B.S. degree in electronic information engineering from the Taiyuan Institute of Technology, in 2017. She is currently pursuing the M.S. degree with the Institute of Lightwave Technology, Beijing Jiaotong University. Her research interests include fiber optics and nonlinear fiber optics.

CHUNCAN WANG received the Ph.D. degree in electronic information engineering from Beijing Jiaotong University, Beijing, China, in 2008. He joined the Key Laboratory of All Optical Network and Advanced Telecommunication Network of EMC, Institute of Lightwave Technology, Beijing Jiaotong University, as a Lecturer, in 2008, where he has been an Associate Professor, since 2010. His research interests include fiber optics, fiber lasers, and nonlinear fiber optics.

CAIPING JIA received the B.S. degree in electronic information engineering from Shaanxi Normal University, in 2017. She is currently pursuing the M.S. degree with the Institute of Lightwave Technology, Beijing Jiaotong University. Her research interests include ultrafast optics and nonlinear fiber optics.

MUGUANG WANG received the B.S. degree in optics from Shandong University, Jinan, China, in 1999, and the Ph.D. degree in electrical engineering from Beijing Jiaotong University, Beijing, China, in 2004. He joined the Key Laboratory of All Optical Network and Advanced Telecommunication Network of EMC, Institute of Lightwave Technology, Beijing Jiaotong University, as a Lecturer, in 2004, where he has been an Associate Professor, since 2006, and a Professor, since 2013.

He was a Visiting Researcher with the Microwave Photonics Research Laboratory, School of Electrical Engineering and Computer Science, University of Ottawa, ON, Canada, in 2012. His current research interests include optical fiber communications and networking, microwave photonics, and optical signal processing.

• • •